Heat Transfer and Boundary Layer Analyses of Laminar and Turbulent Natural Convection in a Cubical Cavity with Differently Heated Opposed Walls.

Alexandre Fabregat[a], Jordi Pallarès[a]

[a] *Departament d'Enginyeria Mecànica*
Universitat Rovira i Virgili (Spain)
Av. Països Catalans, 26, 43007, Tarragona

Abstract

The buoyancy-driven flow in a cubical cavity with differently heated opposed walls has been chosen to investigate the laminar and turbulent heat transfer in enclosed domains. This type of configuration contains the essential physics existing in flows where transport between a fluid and an adjacent solid surface is controlled by the existence of boundary layers. The dependence of the wall heat transfer on the buoyancy force over the range $Ra = 10^5$ to $Ra = 5.4 \times 10^8$ has been investigated, for air ($Pr = 0.7$), using Direct Numerical Simulations. Under the assumption of mixed convection flow within the boundary layer produced by the combined effect of buoyancy and forced convection due to the large-scale flow, we assessed the validity of classical 2D boundary layer solutions in this flow configuration. The resulting characterization of the near-wall flow allows to derive new semi-analytical models for wall transfer applications in enclosed cavities.

Keywords: Thermal boundary layer, Turbulent heat transport, Cavity flow, Direct Numerical Simulation

1. Introduction

Free convection flows in enclosed spaces are commonly encountered in many technological, industrial and natural situations. The efforts to understand the flow behavior and its effects on the heat transfer processes have been important and have produced a vast literature on the topic. Simple geometries, as two-dimensional or three-dimensional parallelepipedic or cylindrical cavities with well-defined thermal boundary conditions, have been used as benchmarks to investigate, in well controlled conditions, the increasing complexity of the flow as the importance of the buoyancy force is increased.

Enclosed Rayleigh-Bénard flows heated from below and side wall heated cavities have been considered as prototypical configurations to analyze laminar, transitional and turbulent free convection flows and their interaction with the thermally active or adiabatic confining walls. Variations of these two reference

Email address: alexandre.fabregat@urv.cat (Alexandre Fabregat)

flow configurations are countless. Some examples of the wide ranges of geometries and boundary conditions considered so far are given in the recent reviews of [5], [11] and [15]. Some of these flow configurations are popular benchmark problems for heat and mass transfer applications [28, 27].

Natural convection in parallelepipedic cavities with simultaneously imposed vertical and horizontal temperature gradients, often referred as mixed cavity free convection, can model thermal conditions inside rooms and exhibition cases of art works. In these situations the vertical temperature gradient can be stable (cold at the bottom and hot at the top) or unstable (hot at the bottom and cold at the top). The relative strength of these two gradients is another additional parameter of the problem.

The stable configuration was analyzed numerically in two dimensional cavities by [19] and [1] and experimentally by [14] and [26]. The effect of the stabilizing vertical temperature gradient on the heat transfer rate depends on its intensity with respect to the horizontal temperature gradient. In the laminar regime, both the horizontal and vertical Nusselt numbers increase in comparison with the case with isothermal horizontal walls at the average temperature [19].

The unstable configuration of the vertical temperature gradient produces surface averaged Nusselt numbers larger on the horizontal walls than in the vertical walls. This arrangement has been analyzed numerically at low Rayleigh numbers ($Ra \leq 10^6$) using two-dimensional simulations ([19, 4, 3]) and experimentally in a cubical cavity ($L = 0.305$ m) filled with water at high Rayleigh numbers ($Ra = \mathcal{O}(10^{10})$) [9]. [23] also considered experimentally this flow setup at $Ra = 5.4 \times 10^8$ and $Ra = 3.6 \times 10^9$ as a representative of the free convection in indoor environments to analyze the particle deposition on the walls of a cubical cavity filled with air ($L = 1.22$ m). At high Rayleigh numbers [7] computed the flow at $Ra = 2.15 \times 10^{10}$ and reported the heat transfer rates in a two-dimensional square cavity solving numerically the Reynolds Averaged Navier-Stokes equations (RANS). This literature review shows that there is a lack of information about the flow and the corresponding heat transfer rates within the range $10^6 < Ra \leq 4 \times 10^9$.

This paper is divided as follows: Section 2 discusses the physical and mathematical models. Results for time-averaged flow fields and heat transfer and comparison of numerical profiles and classical boundary layer solutions for mixed convection are presented in Section 3. Section 4 summarizes the conclusions of this work.

2. Physical and mathematical model

A sketch of the computational domain consisting in a cubical cavity filled with air with coordinate origin located at the center is shown in Fig. 1. The cavity, with a wall side length of $\widetilde{L}$, is heated by imposing a constant temperature $\widetilde{T}_h$ at the bottom $\tilde{y} = -\widetilde{L}/2$ and left $\tilde{x} = -\widetilde{L}/2$ walls (in red) and cooled by imposing a constant temperature $\widetilde{T}_c$ at the top $\tilde{y} = \widetilde{L}/2$ and right $\tilde{x} = \widetilde{L}/2$ walls (in blue). Front and back walls at $\tilde{z} = -\widetilde{L}/2$ and $\tilde{z} = \widetilde{L}/2$ respectively are

considered adiabatic, *i.e.* $\left.\frac{\partial \widetilde{T}}{\partial \widetilde{z}}\right|_{\widetilde{z}=\pm\widetilde{L}/2} = 0$. The temperature difference between the hot and cold walls is $\Delta\widetilde{T} = \widetilde{T}_h - \widetilde{T}_c$. The physical properties of the air at the reference temperature $\widetilde{T}_0 = \frac{\widetilde{T}_h + \widetilde{T}_c}{2}$ are listed in Tab. 1. With the set of values in Tab. 1 and $\Delta\widetilde{T} = 3$ K, the smallest and largest values of the Rayleigh number considered in this work, namely $Ra = 10^5$ and $Ra = 5.4 \times 10^8$, can be attained with cavities of side length $\widetilde{L} = 0.07$ m and $\widetilde{L} = 1.2$ m respectively. Note that the tilde symbol indicates dimensional quantities.

Density	ρ_0	$1.3\ \mathrm{kg\,m^{-3}}$
Kinematic viscosity	ν	$1.57 \times 10^{-5}\ \mathrm{m^2\,s^{-1}}$
Thermal diffusivity	α	$2.24 \times 10^{-5}\ \mathrm{m^2\,s^{-1}}$
Themal expansion coefficient	β	$3.33 \times 10^{-3}\ \mathrm{K^{-1}}$

Table 1: Physical properties of air at $T_0 = 300$ K.

The largest Rayleigh number considered, $Ra = 5.4 \times 10^8$, corresponds to the smallest Ra analyzed experimentally by Thatcher *et al.*[23] who reported measurements of wall particle deposition. This problem will be numerically studied using the present DNS set-up in future investigations.

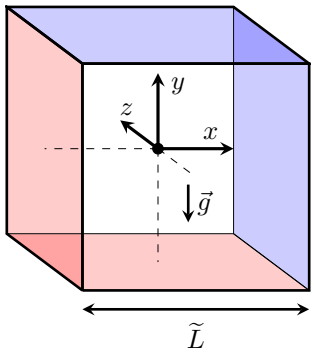

Figure 1: A sketch of the computational domain.

Assuming incompressibility conditions, Boussinesq approximation and negligible radiation effects, the non-dimensional conservation equations for mass, momentum and heat can be written as:

$$\frac{\partial u_i}{\partial x_i} = 0, \tag{1}$$

$$\frac{\partial u_i}{\partial t} + \frac{\partial u_j u_i}{\partial x_j} = -\frac{\partial p}{\partial x_i} + \frac{Pr}{\sqrt{Ra}}\frac{\partial^2 u_i}{\partial x_j \partial x_j} + Pr\theta\delta_{i2}, \tag{2}$$

$$\frac{\partial \theta}{\partial t} + \frac{\partial u_i \theta}{\partial x_i} = \frac{1}{\sqrt{Ra}}\frac{\partial^2 \theta}{\partial x_i \partial x_i}, \tag{3}$$

where u_i are the i-th velocity component in the direction x_i (see Fig. 1), p is the pressure, t is time, g is the magnitude of the gravity acceleration (aligned with $-y$), δ_{ij} is the Kronecker delta and $\theta = T - T_0$ is the temperature perturbation with respect to the reference temperature.

With the Rayleigh and Prandlt numbers defined as $Ra = \frac{g\beta\Delta\widetilde{T}\widetilde{L}^3}{\nu\alpha}$ and $Pr = \nu/\alpha$ respectively, the characteristic length, time, velocity and temperature scales have been chosen to be $\widetilde{L}$, $\frac{\widetilde{L}^2}{\alpha\sqrt{Ra}}$, $\frac{\alpha\sqrt{Ra}}{\widetilde{L}}$ and $\Delta\widetilde{T}$ respectively.

Equations 1-3 have been numerical integrated using the Nek5000 solver [6]. This tool uses a Spectral Element Method (SEM) approach for spatial discretization and a time-adaptive 4-th order Backward Differentiation Formula (BDF) for time integration. Nek5000 has been validated for a wide range of flow configurations on many different computational platforms. The performance results demonstrate an excellent scalability on parallel machines that allows an explicit resolution of a broad range of turbulence spatial and temporal scales.

Along with the temperature boundary conditions of Neumann type at the adiabatic walls, *i.e.* $\frac{\partial\theta}{\partial z}\big|_{z=\pm 1/2} = 0$, and Dirichlet type (constant temperature) at the other walls, *i.e.*$\theta_{y,x=-1/2} = 1/2$ and $\theta_{y,x=1/2} = -1/2$, no-slip boundary conditions have been imposed on every wall. The initial conditions for all the numerical simulations presented here correspond to quiescent, $u_i = 0$, and neutrally buoyant flow, *i.e.*, $\theta = 0$ (or $\widetilde{T} = \widetilde{T_0}$).

The numerical results presented in this work have been obtained by explicitly resolving all the spatial and temporal scales present in the flow. The numerical details for these Direct Numerical Simulations are listed in Tab. 2 including the number of spectral elements in each direction $K = K_x = K_y = K_z$, the order of the polynomial expansion $N = N_x = N_y = N_z$, the total number of mesh points $(K(N+1))^3$ and the minimum and maximum grid spacing $\Delta_{min} = \min(\Delta x) = \min(\Delta y) = \min(\Delta z)$ and $\Delta_{max} = \max(\Delta x) = \max(\Delta y) = \max(\Delta z)$. This resolution meets DNS requirements suggested by Scheel *et al.*for other buoyancy driven flows [16]. Meshes have been constructed to meet the Grötzbach's criterium in Rayleigh-Bénard flows for every mesh element of the grid, this is,

$$\Delta_{max} \leq \pi \left(\frac{Pr^2}{Ra\left(\widehat{Nu}_h - 1\right)} \right)^{1/4} \tag{4}$$

where hat symbol indicates wall average. In addition we ensured a minimum number of 6 grid points within the thermal boundary layer thickness $\delta_t = \left(2\widehat{Nu}\right)^{-1}$. The last column presents the average value of the adaptive time stepping $\langle\Delta t\rangle$ used over the entire simulation. Brackets denote temporal average.

Ra	K	N	$(K(N+1))^3 \times 10^{-6}$	$\Delta_{min} \times 10^4$	$\Delta_{max} \times 10^3$	$\langle \Delta t \rangle \times 10^4$
10^5	8	7	0.26	42.1	37.3	69.1
10^6	9	9	0.28	18.9	28.8	58.4
10^7	13	11	3.79	8.76	16.0	16.5
10^8	16	15	16.8	3.48	9.86	5.8
5.4×10^8	30	13	74.1	2.68	5.75	4.1

Table 2: Mesh details.

3. Results

In the configuration depicted in Fig. 1, the flow will developed a large-scale recirculation in the clockwise direction as seen from the $+z$ direction. This dominant flow feature generates a boundary layer in the vicinity of each non-adiabatic wall. Given the distinct alignment of the gravity vector with respect to the horizontal and vertical walls (normal and parallel respectively), both types of walls will exhibit different boundary layer characteristics.

3.1. Temporal evolution of integral quantities and mean fields

The results discussed in this section correspond to the five different cases listed in Tab. 2 over the range $10^5 \leq Ra \leq 5.4 \times 10^8$. The temporal evolution of the volume-averaged (indicated with an overbar) kinetic energy $\overline{k}$ and dissipation $\overline{\varepsilon}$, defined as:

$$\overline{k} = \frac{1}{2} \int_V (u_i u_i)\, dV, \tag{5}$$

$$\overline{\varepsilon} = \nu \int_V \left(\frac{\partial u_i}{\partial x_j} \frac{\partial u_i}{\partial x_j} \right) dV, \tag{6}$$

respectively, are shown in Fig. 2. The results indicate that, after a transient stage, the flow at $Ra = 10^5$ and $Ra = 10^6$ becomes laminar with the latter case exhibiting a periodic behavior associated to the existence of coherent structures in the flow. In contrast, cases at $Ra = 10^7$, $Ra = 10^8$ and $Ra = 5.4 \times 10^8$ exhibit a fully turbulent regime. Momentum and heat average and turbulent transport fields were collected once the flow reaches a statistically steady regime for $t > 50$.

The average heat flux across a wall can be characterized by the average Nusselt number over its surface $\widehat{Nu}$ which, from dimensional analysis of Fourier's Law [2], can be defined as:

$$\widehat{Nu}_m = -\int_{\Omega_m} \frac{\partial \theta}{\partial n_m} d\Omega_m \tag{7}$$

where $m = \{b, t, l, r, p, q\}$ represent each face of the cubical domain and n_m represent the corresponding face-normal direction. By definition, $\widehat{Nu}_p = \widehat{Nu}_q = 0$ on the adiabatic walls.

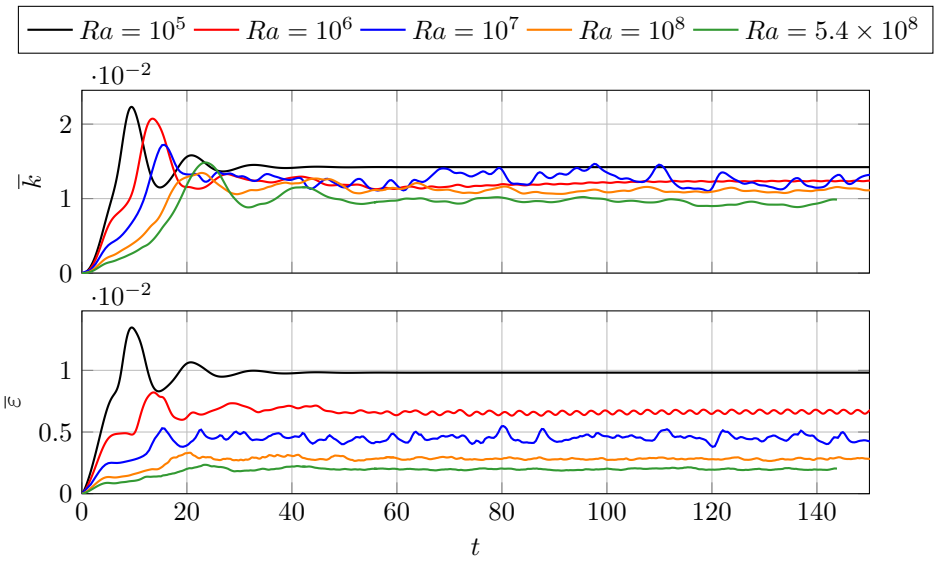

Figure 2: Temporal evolution of volume-averaged kinetic energy and dissipation.

The temporal evolution of the wall-averaged Nusselt number $\widehat{Nu}$ over the time span $50 \leq t \leq 145$ for each case is shown in Fig. 3. The top panel shows the results for the vertical walls with solid and dotted lines for the hot (left) and cold (right) walls. Analogously, the bottom panel shows the $\widehat{Nu}$ results for the horizontal walls with solid and dotted lines for the hot (bottom) and cold (top) wall respectively. The results show that the heat flux enhances as the Rayleigh number increases and that its value is larger for the horizontal walls for all Rayleigh numbers. Fig. 3 also suggests that the flow is statistically developed for times $t > 50$ for all Rayleigh numbers considered.

To illustrate the flow, Fig. 4 shows three slices of instantaneous temperature (a), y-velocity (b), z-velocity (c) and pressure (d) fields at $x = 0.495$, $y = -0.495$ and $z = -0.45$ for the $Ra = 5.4 \times 10^8$ case. The slices in x and y, located within the boundary layer, show the instantaneous structure of the near-wall flow (see Fig. 4(a)-4(b)). The footprint of the dominant clockwise recirculation is clearly illustrated in Figs. 4(b) and 4(d): the air rises along the hot left wall and descends along the opposite right cold wall generating large values of instantaneous pressure at the corners where the flow impinges. The lack of large scale inhomogeneities in the z-velocity field shown in Fig. 4(c) is associated to existence of a $z = 0$ symmetry plane.

The dependence of the vertical (in black) and horizontal (in red) wall Nusselt numbers in the present study is shown in Fig. 5. These results are compared with 2D numerical simulations [19, 4], 3D RANS solutions [7] and experiments [9]. The current 3D numerical results at the two smallest Rayleigh numbers, $Ra = 10^5$ and $Ra = 10^6$, are slightly larger than those found in the 2D simulations

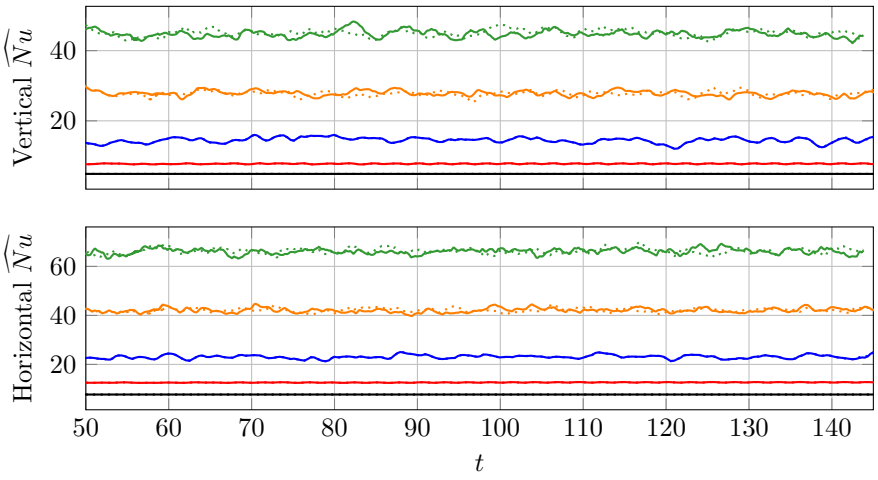

Figure 3: Temporal evolution of the Nusselt numbers on each wall. Solid and dotted lines correspond to hot and cold walls respectively. See legend in Fig. 2

reported by Corcione [4]. When compared with the 2D simulations by Shiralkar and Tien [19], the present work wall-averaged Nusselt values are larger for both the vertical and horizontal walls at $Ra = 10^5$. At $Ra = 10^6$ the values found in [19] deviate significantly from both the present and Corcione [4] results.

As shown in Fig. 5, the results at $Ra = 10^7$, $Ra = 10^8$ and $Ra = 5.4 \times 10^8$ fill an existing gap in the literature. The wall-averaged Nusselt numbers have been fit to the power laws

$$\widehat{Nu}_v = 0.139 Ra^{0.288}, \tag{8}$$

$$\widehat{Nu}_h = 0.317 Ra^{0.266}, \tag{9}$$

for the vertical and horizontal walls respectively. The values of the slopes are relatively close to those found in the experiments by Kirkpatrick and Bohn [9] for values of $Ra > 4.5 \times 10^9$.

3.2. Mean quantities

The time-averaged velocity and temperature perturbation fields at $z = 0$ for the different values of Ra number considered here are shown in Fig. 6 ($z = 0$). The results show the footprint of the clockwise recirculation on the average fields. Although the $z = 0$ symmetry plane should lead to $\lim_{t\to\infty} \langle w \rangle|_{z=0} = 0$, the results for $\langle w \rangle$ at $Ra = 5.4 \times 10^8$ obtained by averaging over the finite time span $50 < t < 145$ exhibit significant values of this velocity component. The lack of symmetry at $Ra = 5.4 \times 10^8$ with respect to $z = 0$ is clearly shown in the other two midplanes at $x = 0$ (Fig. 7) and $y = 0$ (Fig. 8). This asymmetry can be explained by a very low frequency mode in the numerical solution that has not been fully captured in the averaging time span used in the simulation. This type of slow transitions between different dominant Large-Scale Convective

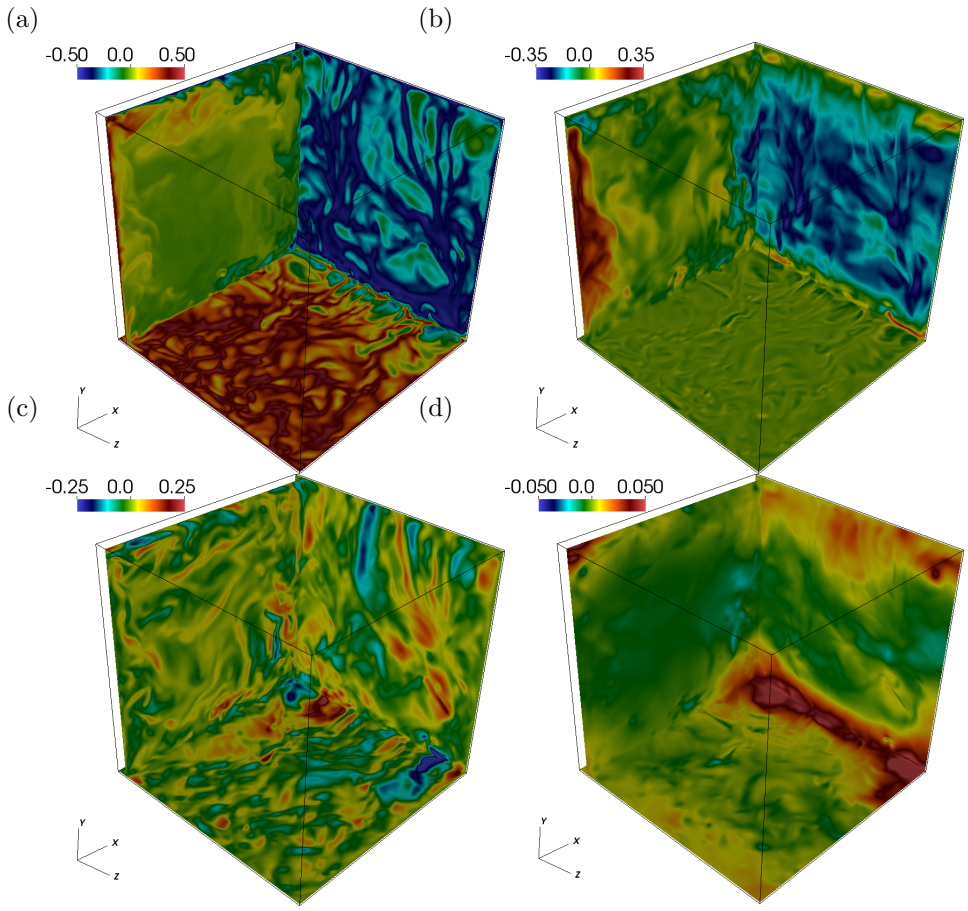

Figure 4: Instantaneous temperature (a), y-velocity (b), z-velocity (c) and pressure (d) fields at $Ra = 5.4 \times 10^8$.

Circulations in buoyancy-driven enclosed flows has previously been observed in Rayleigh-Bénard convection cells [24, 25].

To further illustrate the lack of symmetry of the $Ra = 5.4 \times 10^8$ case, the off-axis time-average fields at $y = 0.45$ are shown in Fig. 9. These results suggest that while the flow at $Ra > 10^8$ is characterized by a mode unity along the z-direction, at $Ra = 5.4 \times 10^8$, the dominant flow feature can exhibit a 3/2-mode in the time-averaged $\langle w \rangle$.

3.3. Structure of the horizontal and vertical boundary layers

In this section we analyze the structure of the momentum and thermal boundary layers on the horizontal and vertical walls. We compare the profiles of velocity and temperature obtained numerically with those predicted by

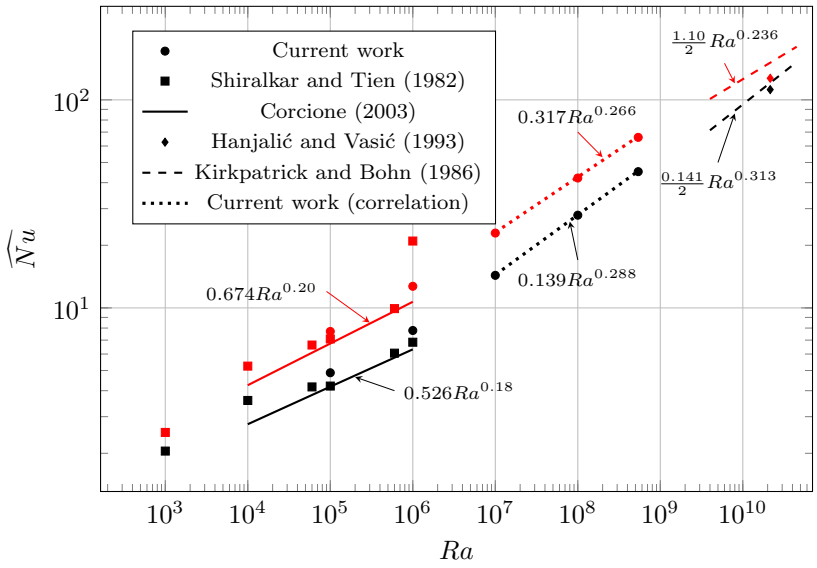

Figure 5: Dependence of the Vertical (black) and Horizontal (red) wall Nusselt numbers on the Rayleigh number in the present study (circles), 2D numerical simulations [19] (squares) and [4] (solid line), 3D RANS solutions [7] (diamonds) and experiments [9] (dashed line).

the classical two dimensional boundary layer theory. The comparison is extended for the local heat transfer rates on the walls. We selected the vertical axis ($x = 0$, $z = 0$) and the horizontal axis ($y = 0$, $z = 0$) of the cubical cavity for the comparison. Figure 10 shows the velocity (top panel) and temperature (bottom panel) along these axes. The data at $Ra \geq 10^6$, for which the flow is unsteady, correspond to time-averaged values.

The models considered are based on the hypothesis of a mixed convection flow within the boundary layer produced by the combined effect of buoyancy and the forced convection effect of the large-scale flow out of the boundary layer. This approach was used by Shi et al (2012) [18] to analyze the horizontal boundary layers in turbulent Rayleigh-Bénard flow in a cylindrical cavity. For the vertical boundary layers we consider a mixed convection Falkner-Skan similar boundary layer [10].

Irrespective of wall considered, we take the s-direction parallel to the wall with the positive s-direction aligned along the main direction of the flow. Thus, $s = 0$ is located at the upstream corner and $s = 1$ at the downstream one. The n-direction is perpendicular to the wall with $n = 0$ at the surface. The governing equations, under the Boussinesq and boundary layer hypotheses, can be written as

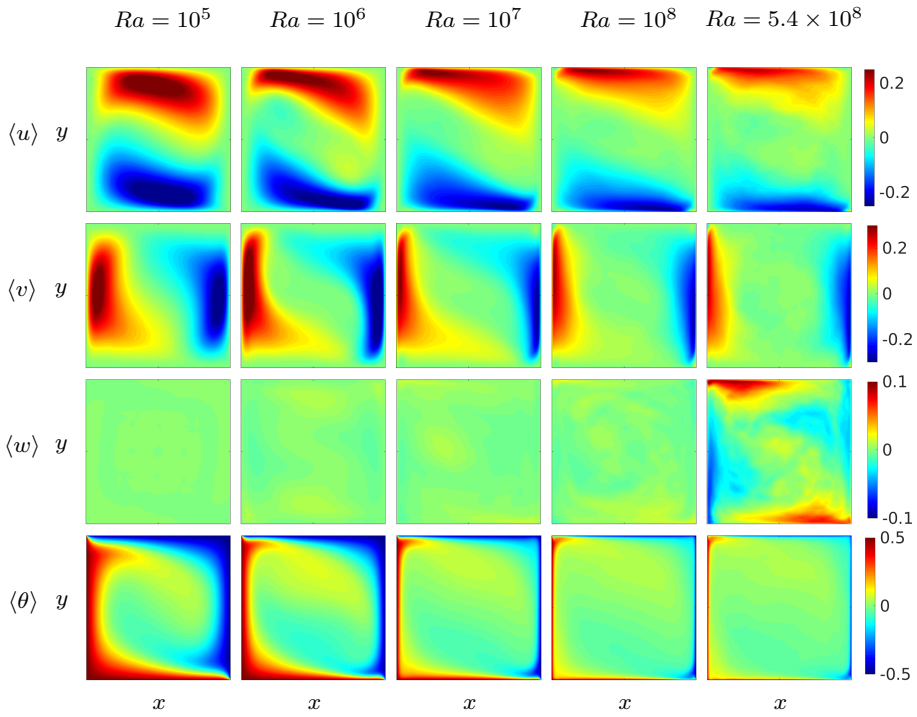

Figure 6: Slice at $z = 0$.

$$\frac{\partial u}{\partial s} + \frac{\partial v}{\partial n} = 0, \tag{10}$$

$$u\frac{\partial u}{\partial s} + v\frac{\partial u}{\partial n} = -\frac{\partial p}{\partial s} + \frac{Pr}{\sqrt{Ra}}\frac{\partial^2 u}{\partial n^2} + Pr\,\theta\,\delta_{sy}, \tag{11}$$

$$0 = -\frac{\partial p}{\partial n} + Pr\,\theta\,\delta_{ny}, \tag{12}$$

$$u\frac{\partial \theta}{\partial s} + v\frac{\partial \theta}{\partial n} = \frac{1}{\sqrt{Ra}}\frac{\partial^2 \theta}{\partial n^2}. \tag{13}$$

In case of horizontal walls s is aligned with the x direction with $s = \frac{1}{2} - x$ for the bottom wall and $s = \frac{1}{2} + x$ for the top wall (see Fig. 1). For the vertical walls s is aligned with the y direction with $s = \frac{1}{2} - y$ for the right wall and $s = \frac{1}{2} + y$ for the left one. According to this, the last term of Eq. (11) is zero for the horizontal boundary layers ($\delta_{sy} = 0$). For the vertical boundary layers ($\delta_{ny} = 0$) Eq. 12 is simplified to $\partial p/\partial n = 0$.

The boundary conditions at the wall ($n = 0$) are $u = 0$, $v = 0$, and $\theta = \theta_w$ ($\theta_w = \frac{1}{2}$ at the hot walls and $\theta_w = -\frac{1}{2}$ at the cold walls). For the horizontal boundary layers, far away from the wall at $n \to \infty$, $\theta = \theta_\infty = 0$ and $u = U_\infty$,

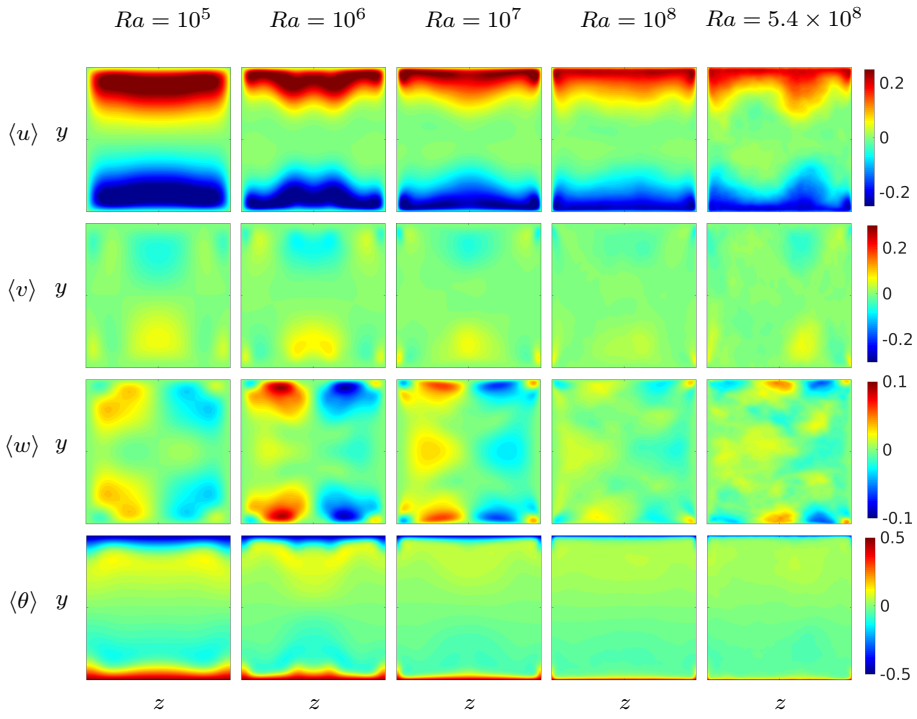

Figure 7: Slice at $x = 0$.

where U_∞ is the velocity out of the boundary layer. For a natural convection, at $n \to \infty$, $\theta = \theta_\infty = 0$ and $u = 0$.

Expansions of the flow velocities (or streamfunction) and temperature can be expressed, for a forced convection flow, as [8]

$$\frac{u(s,n)}{U_\infty} \approx f_0'(\eta) + \epsilon f_1'(\eta) + \epsilon^2 f_2'(\eta) + \cdots \tag{14}$$

$$\Xi(\eta) = \frac{\theta(s,n)}{\theta_w} \approx \Theta_0(\eta) + \epsilon\Theta_1(\eta) + \epsilon^2\Theta_2(\eta) \ldots \tag{15}$$

where η is the similarity variable and f' and Θ are the similar velocity and temperature profiles, respectively. The subindex 0 corresponds to the unperturbed, pure forced convection profiles (Blasius-Pohlhausen solution) and the subindex 1 indicates a linear contribution (perturbation) due to the natural convection. As in Shi et al. (2012) [18], we assume small perturbations ($\epsilon \ll 1$) and we consider only the first two terms of the series.

Similarly, the truncated expansions for a natural convection flow can be written as [18],

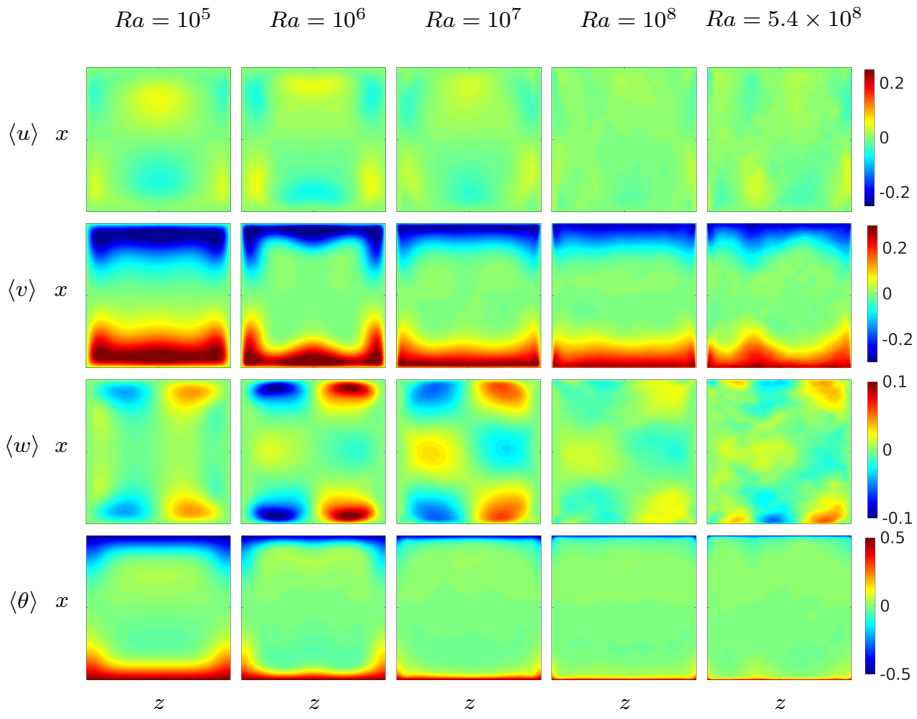

Figure 8: Slice at $y = 0$.

$$\frac{u(s,n)}{U_\infty(s)} \approx g_0'(\eta) + \epsilon g_1'(\eta), \tag{16}$$

$$\Xi(\eta) = \frac{\theta(s,n)}{\theta_w} \approx \chi_0(\eta) + \epsilon \chi_1(\eta). \tag{17}$$

In this case the subindex 0 corresponds to the unperturbed, natural convection profiles of the Stewartson solution for a horizontal boundary layer ([21], [17]) and the subindex 1 indicates the perturbation ($\epsilon \ll 1$) due to the forced convection. The reader can find information about the definition of the similarity variables and the complete sets of ordinary differential equations in Appendix A (Eqs. (A.1) to (A.13)). For the vertical boundary layers, we compare the numerical results with the classical pure natural convection vertical boundary layer [13] and with a mixed convection Falkner-Skan solution [10]. For completeness, the detailed formulations of the pure natural convection and mixed convection boundary layers are included in Appendix A (Eqs. (A.14) to (A.28)).

Figure 11 shows the velocity and temperature boundary layer thicknesses of the profiles shown in Fig. 10. The boundary definition used here corresponds to the distance from the wall where the line with a slope of the gradient at the wall intercepts the extreme value of velocity or temperature outside the boundary

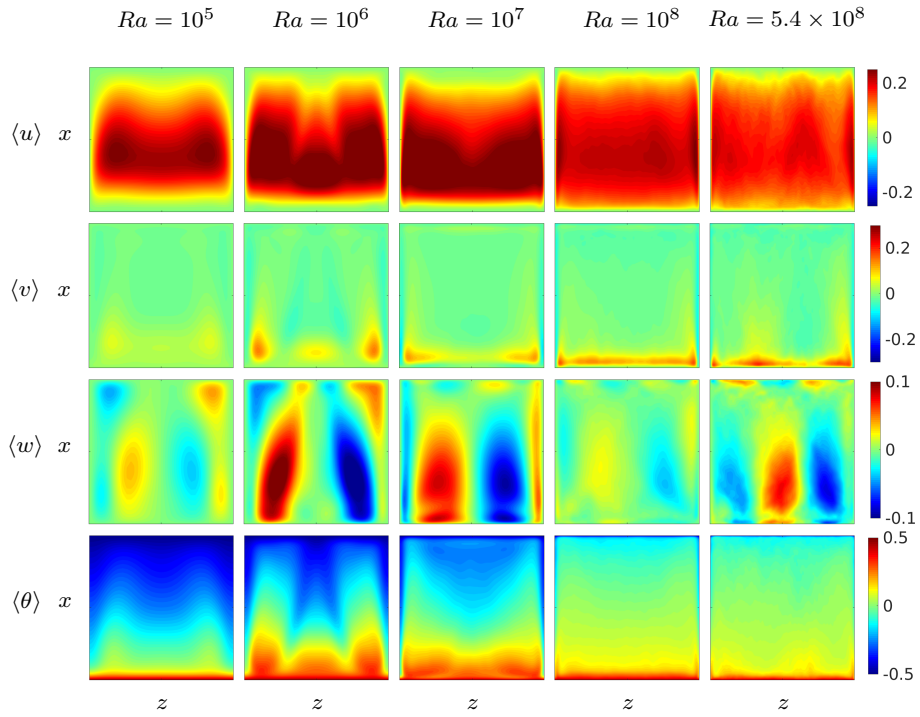

Figure 9: Slice at $y = 0.45$.

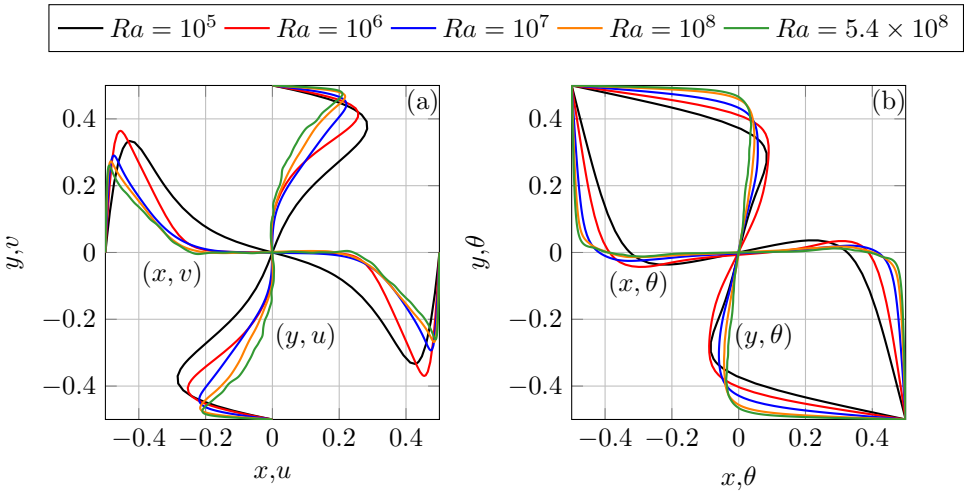

Figure 10: Velocity (left) and temperature (right) profiles along the horizontal and vertical bisectors of the symmetry plane of the cavity z = 0.

layer. It can be seen that the velocity boundary layers at the horizontal wall are about 20% thinner than at the vertical walls in the range of Rayleigh numbers considered. The thermal boundary layers thicknesses are about 4 times larger than the velocity boundary layers. For turbulent flow conditions ($Ra \geq 10^7$) the thermal and momentum boundary layer thicknesses decrease, approximately, as $Ra^{1/3}$ and $Ra^{1/4}$ respectively. Similar trends are found in turbulent Rayleigh-Bénard convection ([22]) and turbulent natural convection in a vertical channel ([12]).

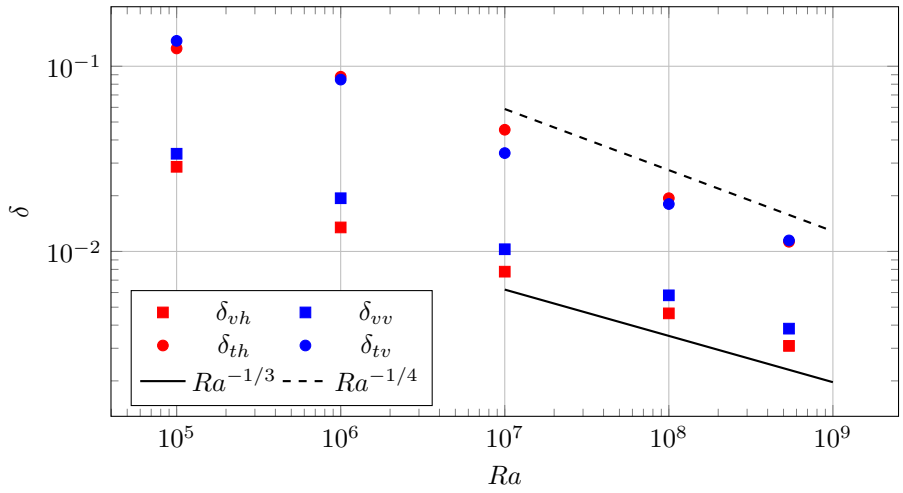

Figure 11: Thermal and velocity boundary layer thickness of the profiles shown in Fig. 10.

3.3.1. Horizontal boundary layers

Figures 12 and 13 show the comparison of the theoretical predictions of the two different types of boundary layers (forced and natural convection) with the profiles of the numerical simulations shown in Fig. 10. These profiles have been scaled with the maximum velocity and the similarity variable η for the numerically predicted profiles has been computed to obtain the same gradient at the wall as the corresponding similar solution. In addition, the profiles near the hot and cold walls have been averaged assuming antisymmetry with respect to the center of the cavity (see Fig. 1).

Figure 12 shows the comparison between the numerical results and the pure ($\epsilon = 0$) forced (Blasius-Pohlhausen, left panels) and natural (Stewartson, right panels) convection boundary layers. Figure 13 shows analogous results of the profiles for forced convection and natural convection boundary layers with small contributions ($\epsilon = 0.075$) of natural and forced convection effects. It can be seen that at $Ra = 10^5$ and $Ra = 10^6$ (laminar flow), the numerical velocity profiles follow a natural convection dominated boundary layer (see Figs. 12(b-1) and 13(b-1)). At larger Rayleigh numbers the flow is turbulent and the velocity boundary layers resemble the theoretical profiles corresponding to a

forced convection flow (see Figs. 12(a-1) and 13(a-1)). As reported by Shi et al. (2012) [18] for Rayleigh-Bénard flow, the numerical predictions depart slightly from the Blasius solution ($\epsilon = 0$) in the range $2 < \eta < 5$ (see Fig. 12(a-1)). It can be seen in Figure 13(a-1) that a forced boundary layer with a small contribution of natural convection ($\epsilon = 0.075$) makes the numerical profiles to collapse with the boundary layer solution. The temperature profiles are less sensitive to the value of ϵ and they show deviations with respect to the theoretical boundary layer predictions for $\eta > 2$.

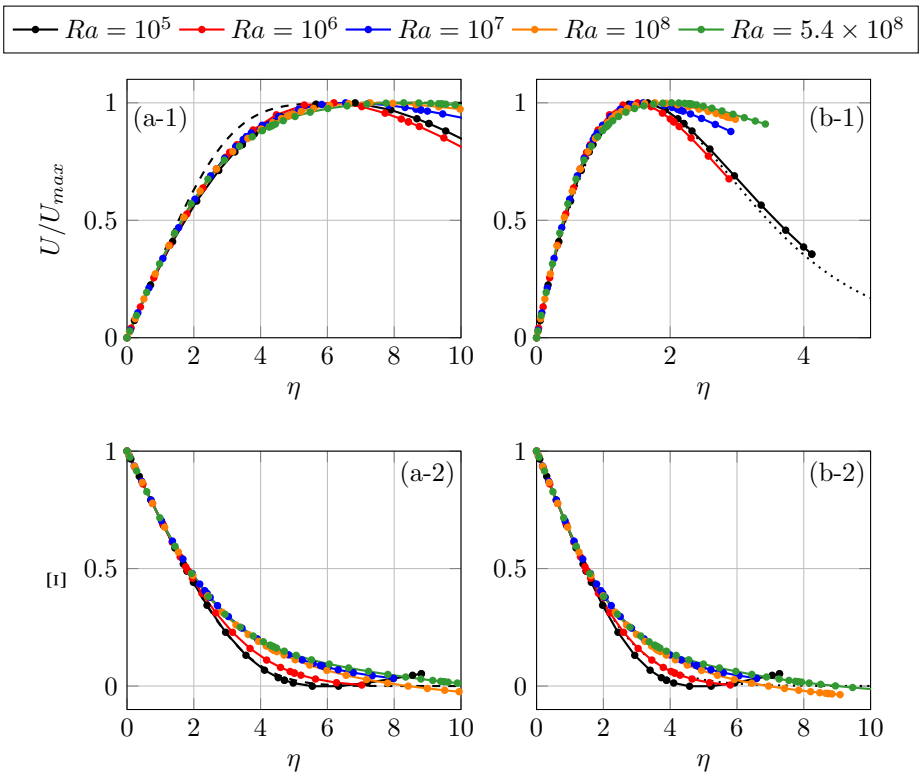

Figure 12: Comparison of the numerical velocity and temperature profiles with classical horizontal boundary layer predictions. (a-1) and (a-2) Pure forced convection. (b-1) and (b-2) Pure natural convection. $\epsilon = 0$

3.3.2. Vertical Boundary layer

The profiles of the vertical boundary layers are plotted in Fig. 14. The theoretical boundary layer profiles shown in Figures 14(a-1) and 14(a-2) correspond to pure natural convection with zero velocity and constant temperature outside the boundary layer and Figures 14(b-1) to 14(b-2) to the Falkner-Skan similar solution boundary layer. The natural convection solution was first reported by Ostrach (1952) [13] and it is also described in Schlichting and Gersten (2017)

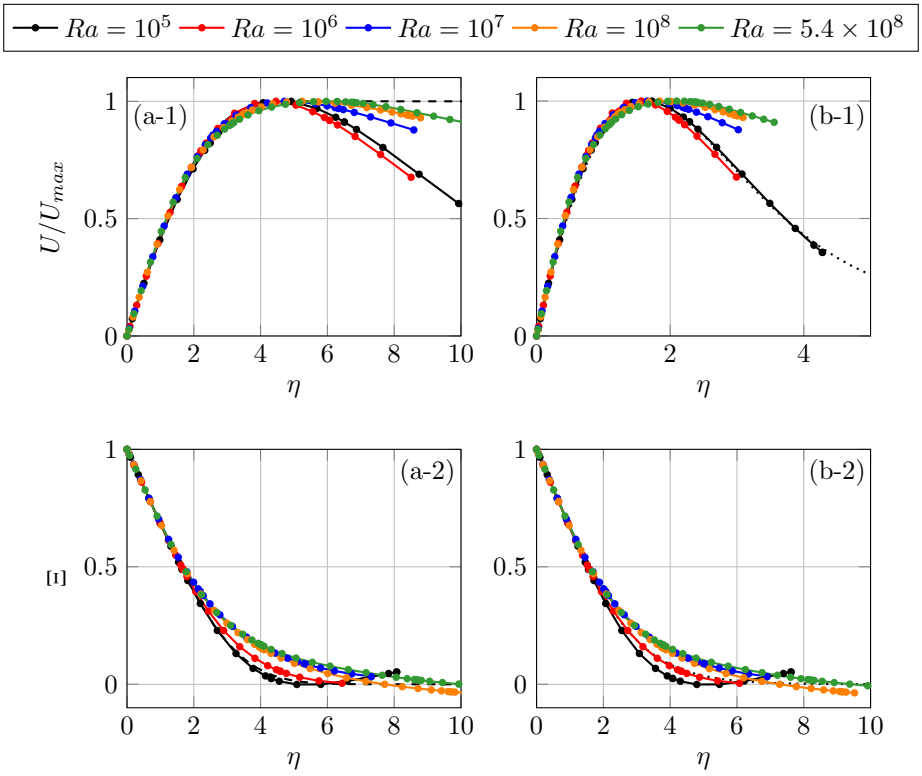

Figure 13: Comparison of the numerical velocity and temperature profiles with classical horizontal boundary layer predictions. (a-1) and (a-2) Forced convection with small natural convection contribution. (b-1) and (b-2) Natural convection with small forced contribution. $\epsilon = 0.075$

[17]. The Falkner-Skan mixed convection boundary layer in a vertical wall is presented and discussed in Merkin (2016) [10].

It can be seen that the numerical velocity profiles agree with the pure natural boundary layer predictions Fig. 14(a-1) for $\eta \leq 1$ independently of the Rayleigh number. At $\eta > 1$ the numerical predictions progressively deviate from the theoretical profile as the Rayleigh number is increased. In fact Fig. 14(a-1) shows that at $Ra = 10^5$ and for $\eta \leq 2$ the velocity boundary layer is well reproduced by the theoretical profile corresponding to a pure natural convection flow. As the Rayleigh number is increased the numerical predictions approach the theoretical mixed-convection profile. For example, at $Ra = 5.4 \times 10^8$ the numerical velocities agree with the Falkner-Skan solution for $\eta \leq 3$. Similarly to the horizontal boundary layers, the numerical temperature profiles exhibit larger deviations with respect the boundary layer similar solutions for $\eta > 1.5$.

In summary, Figures Fig. 12, 13 and 14 indicate that the velocity boundary layers in the cavity are well reproduced by classical laminar boundary layer

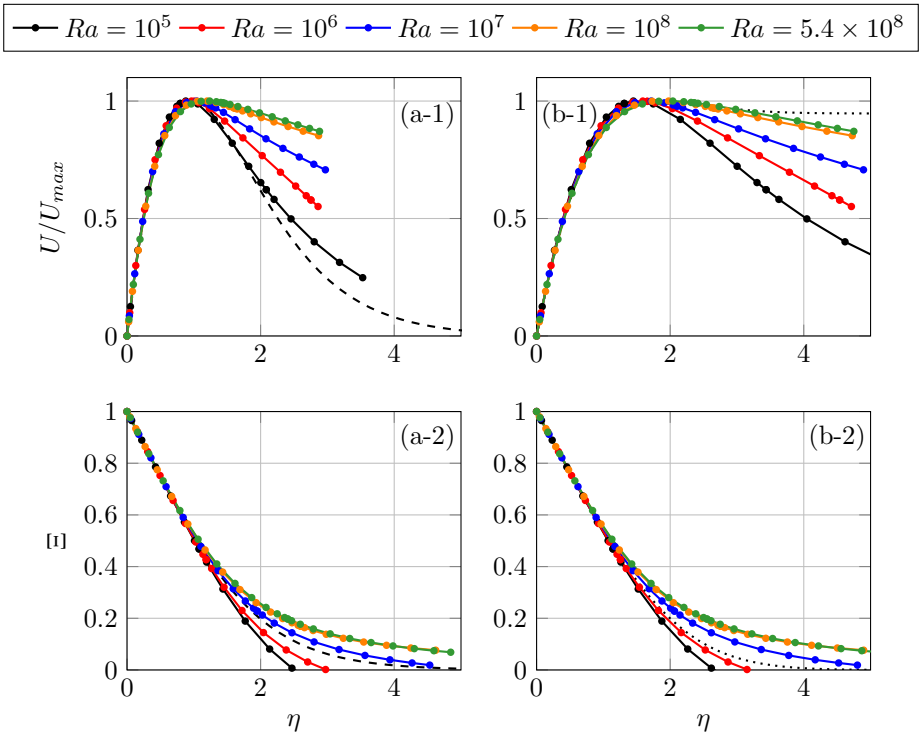

Figure 14: Comparison of the numerical velocity and temperature profiles with classical vertical boundary layer predictions. (a-1) and (a-2) Pure natural convection. (b-1) and (b-2) Falkner- Skan mixed convection.

models, even for Rayleigh numbers for which the flow is turbulent ($Ra \geq 10^7$). At low Ra numbers (laminar flow, $Ra \leq 10^6$) the boundary layers are controlled by pure natural convection effects while at large Ra numbers (turbulent flow) the boundary layers are dominated by the forced convection effect of the large scale flow circulation.

3.3.3. Local Nusselt numbers

Figure 15 shows the local Nusselt numbers along the intersection of the walls with the vertical symmetry plane ($z = 0$) of the cavity. For the horizontal hot wall, the lines correspond to $y = \frac{1}{2}$, $z = 0$ and for the vertical hot wall to $x = \frac{1}{2}$, $z = 0$. Note that in these figures the horizontal axis correspond to the s-direction. The values at the hot and cold walls have been averaged considering antisymmetry with respect to the center of the cavity. For the turbulent flows ($Ra \geq 10^7$) the square mean root of the intensity of the fluctuations of the local Nusselt numbers have been included in Fig. 15 with dashed lines. The theoretical dependences of the local heat transfer coefficients with the position predicted by the boundary layer theories for the horizontal ($Nu_l \propto s^{1/2}$) and vertical ($Nu_l \propto s^{1/4}$) have also been included in Figs. 15(a) and 15(b), re-

spectively. The derivations of these dependences are included at the end of Appendix A. It can be seen that the values of the local Nusselt numbers at different Rayleigh numbers show a relatively good collapse near the center of the walls ($0.2 \leq s \leq 0.8$), if they are scaled with the dependence of the surface averaged Nusselt number on the Rayleigh number. This collapse is more evident at $Ra \geq 10^7$ (turbulent flow) and for the vertical walls (Fig. 15(b)). Figure 15(a) shows that the dependence of the local Nusselt number predicted by the theory for a forced convection dominated boundary layer is well reproduced by the numerical results, especially at the largest Rayleigh number. The intensities of the fluctuations of the local Nusselt number are approximately constant and about 15%-40% of the time averaged values for $s < 0.6$. The fluctuations increase near the corner ($s \approx 1$) where the flow bends towards the vertical wall.

The local Nusselt numbers of the vertical walls (Fig. 15(b)) show, in general, more constant values than those of the horizontal walls. The curves corresponding to turbulent flows ($Ra \geq 10^7$) show a good collapse for $0.1 < s < 0.8$ and the theoretical dependence of the local Nusselt number along the wall agrees well with the numerical predictions.

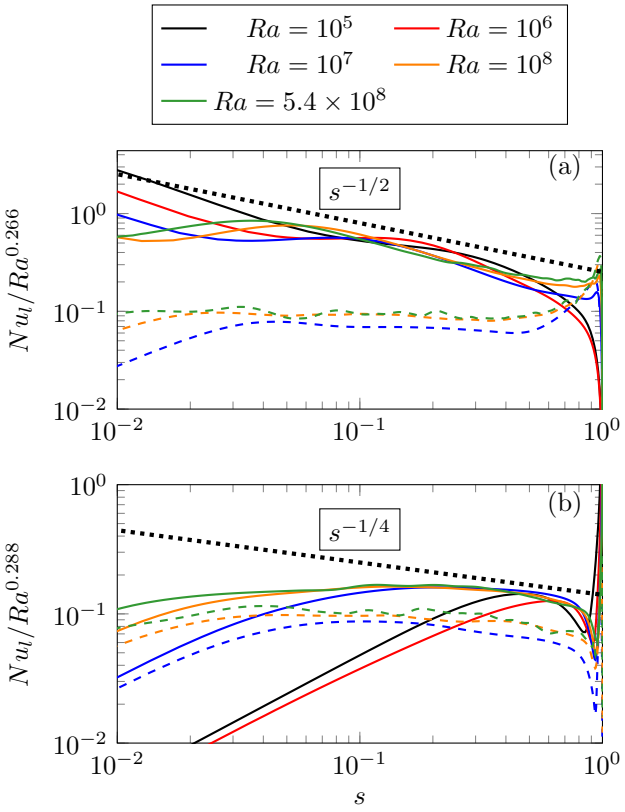

Figure 15: Local Nussel numbers. (a) Horizontal walls. (b) Vertical walls.

4. Conclusions

The time-average wall heat transfer in cavities with thermally opposed walls over the Rayleigh number range $10^5 < Ra < 5.4 \times 10^8$ have been determined via Direct Numerical Simulations. The results allowed to fill the existing gap in the $\widetilde{Nu} \equiv \widetilde{Nu}(Ra)$ curves for this specific configuration. The values of wall Nusselt numbers at $Ra \leq 10^6$ are in good agreement with previously reported results. When compared to available data for higher Rayleigh numbers, the current predictions are in good agreement with experimental measurements carried out at $Ra \sim 10^{10}$.

The time-averaged momentum and thermal fields in the near-wall regions have been compared to classical laminar boundary layer models. The results exhibit notable agreement with the corresponding analytical solutions for both the horizontal and vertical walls even at Rayleigh numbers for which the flow is turbulent ($Ra \geq 10^7$). At low Ra numbers (laminar flow, $Ra \leq 10^6$), the boundary layers are controlled by pure natural convection effects while, at large Ra numbers (turbulent flow), the boundary layers are dominated by the forced convection associated to the outer flow large scale circulation.

Future efforts will be directed to investigate the particle transport and wall deposition at $Ra = 5.4 \times 10^8$ presented here. Wall deposition rate results will be compared to available experiments reported in the literature at the same Rayleigh number.

5. Acknowledgements

This work has been funded by Spanish Ministerio de Ciencia, Innovación y Universidades through the grants DPI2016-75791-C2-1-P and RTI2018-100907-A-I00 (MCIU/AEI/FEDER, UE) and also by the Generalitat de Catalunya through the grant 2017-SGR-1234.

[1] F. Arpino, N. Massarotti, and A. Mauro. High Rayleigh number laminar-free convection in cavities: New benchmark solutions. *Numerical Heat Transfer, Part B: Fundamentals*, 58(2):73–97, 2010.

[2] T. L. Bergman, A. S. Lavine, F. P. Incropera, and D. P. DeWitt. *Fundamentals of Heat and Mass Transfer*. John Wiley & Sons, 8 edition, 2018.

[3] C. Cianfrini, M. Corcione, and P. P. Dell'Omo. Natural convection in tilted square cavities with differentially heated opposite walls. *International Journal of Thermal Sciences*, 44(5):441 – 451, 2005.

[4] M. Corcione. Effects of the thermal boundary conditions at the sidewalls upon natural convection in rectangular enclosures heated from below and cooled from above. *International Journal of Thermal Sciences*, 42(2):199 – 208, 2003.

[5] D. Das, M. Roy, and T. Basak. Studies on natural convection within enclosures of various (non-square) shapes a review. *International Journal of Heat and Mass Transfer*, 106:356 – 406, 2017.

[6] P. F. Fischer, J. W. Lottes, and S. G. Kerkemeier. Nek5000 Web page, 2008. http://nek5000.mcs.anl.gov.

[7] K. Hanjalić and S. Vasić. Computation of turbulent natural convection in rectangular enclosures with an algebraic flux model. *International Journal of Heat and Mass Transfer*, 36(14):3603 – 3624, 1993.

[8] C. A. Hieber. Mixed convection above a heated horizontal surface. *International Journal of Heat and Mass Transfer*, 16:769–785, 04 1973.

[9] A.T. Kirkpatrick and M. Bohn. An experimental investigation of mixed cavity natural convection in the high Rayleigh number regime. *International Journal of Heat and Mass Transfer*, 29(1):69 – 82, 1986.

[10] J. H. Merkin. Mixed convection in a Falkner–Skan system. *Journal of Engineering Mathematics*, 100(1):167–185, 2016.

[11] I.V. Miroshnichenko and M.A. Sheremet. Turbulent natural convection heat transfer in rectangular enclosures using experimental and numerical approaches: A review. *Renewable and Sustainable Energy Reviews*, 82:40 – 59, 2018.

[12] C. S. Ng, A. Ooi, D. Lohse, and D. Chung. Vertical natural convection: application of the unifying theory of thermal convection. *Journal of Fluid Mechanics*, 764:349361, 2015.

[13] S. S. Ostrach. An analysis of laminar free-convection flow and heat transfer about a flat plate paralled to the direction of the generating body force. Technical report, Lewis Flight Propulsion Lab., 1953.

[14] S. S. Ostrach and C.C. Raghavan. Effect of stabilizing thermal gradients on natural convection in rectangular enclosures. *ASME. J. Heat Transfer*, 101:238–243, 1979.

[15] S. Pandey, Y. G. Park, and M. Y. Ha. An exhaustive review of studies on natural convection in enclosures with and without internal bodies of various shapes. *International Journal of Heat and Mass Transfer*, 138:762 – 795, 2019.

[16] J. D. Scheel, M. S. Emran, and J. Schumacher. Resolving the fine-scale structure in turbulent Rayleigh–Bénard convection. *New Journal of Physics*, 15(11):113063, 2013.

[17] H. Schlichting and K. Gersten. *Boundary-Layer Theory*. Springer-Verlag Berlin Heidelberg, 9 edition, 2017.

[18] N. Shi, M. S. Emran, and J. Schumacher. Boundary layer structure in turbulent Rayleigh-Bénard convection. *Journal of Fluid Mechanics*, 706:533, 2012.

[19] G. S. Shiralkar and C. L. Tien. A numerical study of the effect of a vertical temperature difference imposed on a horizontal enclosure. *Numerical Heat Transfer*, 5(2):185–197, 1982.

[20] O. Shishkina. Momentum and heat transport scalings in laminar vertical convection. *Phys. Rev. E*, 93:051102, May 2016.

[21] K. Stewartson. On the free convection from a horizontal plate. *Zeitschrift Angewandte Mathematik und Physik*, 9:276–282, 1958.

[22] C. Sun, Y.-H. Cheung, and K.-Q. Xia. Experimental studies of the viscous boundary layer properties in turbulent Rayleigh-Bénard convection. *Journal of Fluid Mechanics*, 605:79113, 2008.

[23] T. L. Thatcher, W. A. Fairchild, and W. W. Nazaroff. Particle deposition from natural convection enclosure flow onto smooth surfaces. *Aerosol Science and Technology*, 25(4):359–374, 1996.

[24] L. Valencia, J. Pallarès, I. Cuesta, and F. X. Grau. Turbulent rayleighbnard convection of water in cubical cavities: A numerical and experimental study. *International Journal of Heat and Mass Transfer*, 50(15):3203 – 3215, 2007.

[25] A. Vasiliev, P. Frick, A. Kumar, R. Stepanov, A. Sukhanovskii, and M.K. Verma. Transient flows and reorientations of large-scale convection in a cubic cell. *International Communications in Heat and Mass Transfer*, 108:104319, 2019.

[26] W. Wu and C. Y. Ching. The effect of the top wall temperature on the laminar natural convection in rectangular cavities with different aspect ratios. *ASME. J. Heat Transfer*, 131:052501–052501–11, 2009.

[27] A. Xu, L. Shi, and H.-D. Xi. Lattice boltzmann simulations of three-dimensional thermal convective flows at high rayleigh number. *International Journal of Heat and Mass Transfer*, 140:359 – 370, 2019.

[28] A. Xu, L. Shi, and T.S. Zhao. Accelerated lattice boltzmann simulation using gpu and openacc with data management. *International Journal of Heat and Mass Transfer*, 109:577 – 588, 2017.

Appendix A.

In this appendix we report, for completeness, the mathematical models (governing equations and definition of the similarity variables) of the classical two dimensional boundary layers considered for the comparison with the DNS results. The theoretical dependences of the local Nusselt number along the wall are also included at the end of this appendix. The hypotheses, common to all the cases, are: constant gravity and wall temperature, validity of the Boussinesq approximation and negligible radiation and viscous dissipation effects. The x-direction is parallel to the wall and the y-direction is perpendicular to the wall. The wall is located at $y = 0$ and has dimension L.

Governing equations for horizontal boundary layers

For the horizontal boundary layers, we follow the perturbative expansion of the equations reported in Shi *et al.*(2012) [18]. In this approach the boundary layer is assumed to be governed mainly by forced convection or, alternatively, by natural convection. A small linear contribution is added to the dependent variables (streamfunction and temperature) to model the effect natural convection in a forced convection boundary layer or, alternatively, the effect of forced convection in a natural convection boundary layer (see Eqs. (14) and (15)). The definition of the similarity variable, η, and the expansion parameter, ϵ, are, for a forced convection boundary layer

$$\eta = \frac{y}{x} Re_x^{1/2} \text{ and } \epsilon = Gr_x/Re_x^{5/2} \tag{A.1}$$

and for a natural convection boundary layer

$$\eta = \frac{y}{x} Gr_x^{1/5} \text{ and } \epsilon = Re_x/Gr_x^{2/5}. \tag{A.2}$$

The introduction of the definitions of Eqs.(14) to (17) and Eqs.(A.1) and (A.2) into the governing equations leads to the following sets of ordinary differential equations. For forced convection the base flow is governed by

$$f_0''' + \frac{1}{2} f_0'' f_0 = 0, \tag{A.3}$$

$$\Theta_0'' + \frac{Pr}{2} f_0 \Theta_0' = 0, \tag{A.4}$$

with boundary conditions: at $\eta = 0$, $f_0 = f_0' = 0$ and $\Theta_0 = 1$ and for $\eta \to \infty$, $f_0' = 1$ and $\Theta_0 = 0$. For the forced convection flow, the natural convection perturbation is governed by

$$f_1''' + f_0'' f_1 + \frac{1}{2} f_0 f_1'' - \frac{1}{2} f_0' f_1' - \frac{1}{2} h_0 + \frac{\eta}{2} h_0' = 0, \tag{A.5}$$

$$h_0' = \Theta_0, \tag{A.6}$$

$$\Theta_1'' + \frac{Pr}{2} f_0 \Theta_1' - \frac{Pr}{2} f_0' \Theta_1 + Pr \Theta_0' f_1 = 0, \tag{A.7}$$

with boundary conditions: at $\eta = 0$, $f_1 = f_1' = 0$ and $\Theta_1 = 0$ and for $\eta \to \infty$, $f_1' = \Theta_1 = h_0 = 0$. The term h_0' arise from the pressure term. For a natural convection boundary layer the base flow is governed by

$$g_0''' + \frac{3}{5} g_0'' g_0 - \frac{1}{5} \left(g_0'\right)^2 - \frac{2}{5} k_0 + \frac{2}{5} \eta k_0' = 0, \tag{A.8}$$

$$k_0' = \chi_0, \tag{A.9}$$

$$\chi_0'' + \frac{3Pr}{5} g_0 \chi_0' = 0, \tag{A.10}$$

with boundary conditions: at $\eta = 0$, $g_0 = g_0' = 0$ and $\Xi_0 = 1$ and for $\eta \to \infty$, $g_0' = \Xi_0 = k_0 = 0$. For the natural convection flow, the forced convection perturbation is governed by

$$g_1''' + \frac{3}{5} g_1'' g_0 - \frac{1}{5} g_1' g_0' + \frac{2}{5} g_0'' g_1 - \frac{1}{5} k_1 + \frac{2}{5} \eta k_1' = 0, \tag{A.11}$$

$$k_1' = \chi_1, \tag{A.12}$$

$$\chi_1'' + \frac{3Pr}{5} g_0 \chi_1' + \frac{Pr}{5} g_0' \chi_1 + \frac{2Pr}{5} \chi_0' g_1 = 0, \tag{A.13}$$

with boundary conditions: at $\eta = 0$, $g_1 = g_1' = \Xi_1 = 0$ and for $\eta \to \infty$, $\Xi_1 = k_1 = 0$ and $g_1' = 1$. Again, k_0 and k_1 arise from the pressure term.

Governing equations for vertical boundary layers

The laminar steady pure natural convection boundary layer flow near an isothermal vertical wall was analyzed by Ostrach (1953) [13] and it is also described in Bergman et al. (2011) [2].

Considering the following similarity variables

$$\eta = \frac{y}{x} \left(Gr_x/4\right)^{1/4}, \tag{A.14}$$

$$\mathrm{F}(\eta) = \psi / \left[4\nu \left(Gr_x/4\right)^{1/4}\right], \tag{A.15}$$

$$\Xi(\eta) = \frac{\theta(s,n)}{\theta_w}, \tag{A.16}$$

the boundary layer equations can be written as

$$\mathrm{F}''' + 3\mathrm{F}\mathrm{F}'' - 2\mathrm{F}^2 + \Theta = 0, \tag{A.17}$$

$$\Theta'' + 3\,\mathrm{Pr}\,\mathrm{F}\Theta' = 0, \tag{A.18}$$

with boundary conditions: at $\eta = 0$, $F = F' = 0$ and $\Theta = 1$ and for $\eta \to \infty$, $F' = 0$ and $\Theta = 0$.

The effect of a large scale flow in vertical pure natural convection boundary layers has been investigated by Shishkina (2016) [20]. Here we consider the effect of the bulk flow on the vertical boundary layers by imposing a wind far away from the wall. In order to express the boundary layer equations in terms of similarity variables, we adopt Falkner-Skan velocity and temperature profiles out of the boundary layer ($y \to \infty$) of the form (Merkin, 2016) [10].

$$U_\infty(x) = \widetilde{U}(x/L)^m, \tag{A.19}$$

$$T_\infty - T_w(x) = \widetilde{T}(x/L)^{2m-1}. \tag{A.20}$$

Since the wall temperature is constant in the vertical boundary layers of the cavity, $m = 1/2$ and consequently the velocity far from the wall is assumed to be $U_\infty(x) = \widetilde{U}(x/L)^{1/2}$. As we particularize the solution for a constant temperature increment (i.e. $m = 1/2$) then $\widetilde{T} = T_w - T_\infty = \Delta T_{1/2}$.

We can define the following non-dimensional variables

$$\Psi = LRe^{-1/2}\widetilde{U}\Psi^{**}, \tag{A.21}$$

$$T - T_\infty = \Delta T_{1/2} T^{**}, \tag{A.22}$$

$$x = Lx^*, \tag{A.23}$$

$$y = Re^{-1/2} L y^{**}, \tag{A.24}$$

with $Re = \widetilde{U}L/\nu$.

The similarity variables, F, Θ and η are defined as

$$F = \Psi^{**}(x^*)^{-3/4}, \tag{A.25}$$

$$\Theta = T^{**} Ri_{1/2} = \Xi(\eta), \tag{A.26}$$

$$\eta = y^{**}(x^{**})^{-1/2}, \tag{A.27}$$

where $Ri_{1/2}$ is the Richardson number, $Ri_{1/2} = Ra_{1/2}Re^2 = \frac{g\beta\Delta T_{1/2}L}{U_0}$. The introduction of these definitions into the 2D boundary layer equations results in the following system of ordinary differential equations.

$$\mathrm{F}''' + \frac{3}{4}\mathrm{F}\mathrm{F}'' + \frac{1}{2}\left(1 - \mathrm{F}^2\right) + \Theta = 0, \tag{A.28}$$

$$\Theta'' + \frac{3}{4}\,\mathrm{Pr}\,\mathrm{F}\Theta' = 0, \tag{A.29}$$

with boundary conditions: at $\eta = 0$, $F = F' = 0$ and $\Theta = 1$ and for $\eta \to \infty$, $F' = 1$ and $\Theta = 0$.

Theoretical dependences of the local Nusselt number

The local Nusselt number Nu_l can be defined as

$$Nu_l = -\left.\frac{\partial T}{\partial y}\right|_{y=0} \frac{L}{\Delta T} = -\left.\frac{\partial \Xi(\eta)}{\partial \eta}\right|_{y=0} \frac{\partial \eta}{\partial y}. \tag{A.30}$$

For a horizontal boundary layer governed by a forced convection flow ($\epsilon = 0$) the dependence of the local Nusselt number with the position along the wall is

$$Nu_l \propto x^{-1/2} \tag{A.31}$$

and for a horizontal natural convection boundary layer ($\epsilon = 0$),

$$Nu_l \propto x^{-4/5}. \tag{A.32}$$

For a vertical pure natural convection boundary layer and for a mixed convection Falkner-Skan flow

$$Nu_l \propto x^{-1/4}. \tag{A.33}$$